Journal of Magnetic Resonance 389 (2026) 108089

Contents lists available at ScienceDirect

Journal of Magnetic Resonance

journal homepage: www.elsevier.com/locate/jmr

In situ time-resolved motion of a tethered *Pachnoda marginata*, AI-correlated using μMRI and optical imaging

Ajmal Chenakkara [a], Mazin Jouda [a], Ulrike Wallrabe [b], Jan G. Korvink [a,*]

[a] Institute of Microstructure Technology (IMT), Karlsruhe Institute of Technology (KIT), Germany
[b] Institute of Microsystem Technology (IMTEK), University of Freiburg, Germany

ARTICLE INFO

Dataset link: https://github.com/chenakkara/Treadmill_dynamic_MRI.git

Keywords:
In-situ treadmill
Tethered insect imaging
Deep learning undersampling correction
View-shared reconstruction
Dynamic μMRI

ABSTRACT

Microscopic magnetic resonance imaging (μMRI) is a versatile, non-invasive imaging modality and a potential candidate for studying the internal biomechanics associated with locomotion of small, freely behaving invertebrate model organisms. However, conventional μMRI acquisition is inherently sequential and relatively slow, limiting its ability to capture the locomotion and physiological dynamics of insects that occur on much faster timescales. In our previous work, we introduced an *in situ* spherical treadmill setup with integrated optical imaging system compatible with an ultra-high-field magnet, enabling motion-compensated imaging of tethered active insects. Here, we extend this platform by developing an accelerated μMRI acquisition scheme for dynamic insect biomechanics. As a proof-of-concept, we evaluate the feasibility of optimizing a RARE (fast spin-echo) sequence for imaging the relatively slow dynamics of a behaving sun beetle (*Pachnoda marginata*). The proposed method uses a dynamic undersampling strategy to accelerate acquisition, combined with retrospective view-sharing to partially fill k-space and exploit temporal redundancies. A deep learning module further refines the images by correcting the resultant undersampling artifacts. This integrated framework enables correlated time-resolved μMRI and optical imaging of a tethered active insect, broadening the capabilities of non-invasive biomechanical studies in small, behaving organisms.

1. Introduction

Investigating freely moving model organisms is fundamental to advancing our understanding of the connection between biological function and behavior. Dynamic imaging plays a central role in such studies, enabling the visualization of motion and body deformation in living systems. A range of imaging modalities, including optical [1,2] and X-ray techniques [3,4], have been widely employed to capture motion across diverse spatial and temporal scales. Alternatively, micro magnetic resonance imaging (μMRI) provides a uniquely powerful, non-invasive means of probing soft biological tissues, offering high contrast and detailed structural and functional information. However, the inherently sequential and relatively slow nature of MRI acquisition poses substantial challenges for dynamic imaging, particularly when capturing the rapid, complex, and irregular motions characteristic of freely behaving small organisms.

Recently, we introduced an *in situ* treadmill setup with an integrated MR-compatible optical imaging system [5,6] for motion-compensated imaging of a tethered behaving insect. This platform provides an effective, non-invasive method for visualizing internal structures during tethered locomotion in insect-sized model organisms. However, insect locomotion is often highly irregular, making it challenging to apply conventional gating-based MRI methods to visualize true body dynamics with sufficient spatio-temporal resolution. Fast dynamic MRI techniques offer a promising alternative, as demonstrated in various preclinical and clinical applications [7,8]. Advances in hardware and reconstruction algorithms have enabled dynamic MRI to achieve real-time imaging of rapid physiological processes, making it increasingly valuable for studies requiring both high spatial and temporal resolution [9–11]. In this study, we investigate the feasibility of accelerating dynamic 2D μMRI within the constraints of a single-coil acquisition in a tethered, active insect, with the goal of visualizing the abdominal stride patterns associated with locomotion.

Deep learning-based methods have emerged as the state-of-the-art for accelerated MRI, spanning the full pipeline from acquisition to reconstruction [12,13]. A wide range of architectures have been proposed, and U-Net [14] derived supervised image-to-image translation networks continue to serve as strong baselines for undersampled reconstruction. The scarcity of training data for both clinical and preclinical MRI remains a significant challenge. This issue is even more pronounced in the μMRI domain, owing to the uniqueness of the animal

* Corresponding author.
E-mail address: jan.korvink@kit.edu (J.G. Korvink).

https://doi.org/10.1016/j.jmr.2026.108089
Received 23 December 2025; Received in revised form 7 April 2026; Accepted 12 May 2026
Available online 21 May 2026

models or samples employed. In our previous study, we addressed this limitation through a transfer learning approach [6] for the case of MRI motion artifact correction of tethered active insect. In the present work, we extend this methodology to the problem of undersampled MRI reconstruction.

The degree of undersampling, and consequently the achievable acceleration in dynamic MRI, is tightly coupled to the desired spatiotemporal resolution. Excessive undersampling can degrade reconstruction quality, particularly when deep learning is applied only as a post-hoc artifact correction step. View-sharing is an MRI interpolation technique that reconstructs missing k-space data by exploiting information from neighboring acquisitions. It is often integrated with undersampling strategies to reduce scan time [15–17], and thereby enhancing the apparent temporal resolution for dynamic imaging. This capability has proven particularly valuable in dynamic imaging applications, such as cardiac and contrast-enhanced studies, where rapid acquisition is essential [18,19]. However, aggressive view-sharing can introduce temporal blurring and motion-related artifacts when inconsistencies arise with the true underlying dynamics. Integrating compressed sensing (CS) reconstruction with view-sharing has been shown to reduce the temporal footprint and associated blurring. Restricting view-sharing to a small region of k-space, typically the most recent neighboring lines and reconstructing the remaining undersampled data with CS shortens the effective temporal footprint without compromising image quality [20,21]. In the present work, we extend this concept by replacing the CS reconstruction with a deep learning module, enabling rapid reconstructions with improved image quality. We propose a hybrid reconstruction framework that first employs view-sharing to coherently augment the undersampled k-space data, and then applies a deep learning module as a postprocessing step to correct remaining undersampling artifacts, enhancing the fidelity of dynamic images. This approach improves the temporal resolution required for *in vivo* μMRI characterization of the abdominal pitching motion in tethered *Pachnoda marginata*, while simultaneously enabling correlated, time-resolved optical imaging, with potential to inform future studies of behavior and biomechanics.

2. Methodology

2.1. Experimental setup

We developed an *in situ* treadmill setup with an integrated optical imaging system for motion-compensated μMRI of an active *Pachnoda marginata* inside a 15.2 T ultra-high-field magnet (Bruker Biospin, Ettlingen, Germany) [5]. A detailed description of the system's design and operation is provided in [5]. The system incorporates a 3D-printed tethering assembly that stabilizes the insect within the bore while maintaining minimal restraint, enabling MRI of actively behaving specimens. It is integrated with a commercial 35 mm inner-diameter quadrature ^1H birdcage RF volume coil (Bruker Biospin, Ettlingen, Germany) tuned to 650 MHz, as illustrated in Fig. 1(a–c). An MR-compatible optical imaging system has also been integrated within the bore (details available in [5]) to enable correlated imaging of external morphological dynamics of the insect during tethered locomotion.

2.2. k-space undersampling and view-sharing

We used single-coil Cartesian undersampling to acquire single-slice 2D sagittal MRI temporal frames. The k-space was undersampled according to the schematic shown in Fig. 2. For each 200 × 200 k-space frame, the central 60 phase-encode lines were fully sampled to capture low-frequency information, complemented by 20 peripheral phase-encode lines randomly selected, with each of the 7 consecutive frames having a unique peripheral sampling pattern. This variable-density random sampling with a fully sampled center favors preservation of low-frequency information, such that undersampling artifacts manifest primarily as blurring rather than aliasing. A RARE (Rapid Acquisition with Relaxation Enhancement) [22] sequence available in *Paravision 360v3* (Bruker BioSpin, Ettlingen, Germany) was modified to support acquisition with a custom phase-encoding table for each frame.

Acquisition parameters were: repetition time (TR) = 150 ms, echo time (TE) = 5 ms, RARE factor = 10, field of view (FOV) = 30 mm × 30 mm, undersampled matrix size = 80 × 200, in-plane resolution = 150 µm × 150 µm, slice thickness = 0.7 mm, repetitions = 140, no signal averaging, acquisition time of 1.2 s per frame, and a total acquisition time of 168 s, corresponding to an effective acceleration factor of R = 2.5. The sequence parameters and undersampling design were selected to favor better spatial resolution and temporal efficiency for depicting internal morphology, rather than optimizing for conventional tissue contrast. The resulting atypical contrast is adequate for resolving the structural features examined in this study.

Retrospective view-sharing was implemented by incorporating peripheral k-space lines from the two frames preceding and the two frames following each target frame (i.e., frames $n-2$ through $n+2$) to increase the effective data density per frame (Fig. 2(a–c) shows the case for $n-1$ and $n+1$). The resulting k-space was then processed using the discrete fast Fourier transform to produce the reconstructed MR images (Fig. 2(d)). The view-sharing reconstruction has been implemented using custom MATLAB (MathWorks, Natick, MA, USA, R2024b) scripts. The resulting reconstructions contained undersampling artifacts, which were subsequently corrected using a deep learning model as a downstream processing step (Fig. 2(e)).

2.3. Deep learning for undersampled MRI artifact correction

2.3.1. Datasets

We used the same ground-truth datasets as in our previous work on μMRI motion artifact removal [6]. Here, they were repurposed to generate paired training images for undersampling artifact correction. Two fully sampled datasets were used. The first was a publicly available T1–weighted adult human brain MRI dataset [23], acquired with a 12-channel coil and normalized to a single complex-valued image set of size 256 × 256, from which a subset of 3750 unique images was used. The second consisted of 200 sagittal MRI slices of inactive insects (Fig. 1(e)), acquired on a 15.2 T Bruker system with a 35 mm quadrature ^1H birdcage coil using RARE sequence. Imaging parameters were TR = 500 ms, TE = 5 ms, matrix size = 256 × 256 pixels, FOV = 30 mm × 30 mm, in-plane resolution = 117 µm × 117 µm, slice thickness = 1 mm, no averaging, RARE factor = 4, and acquisition time of 32 s for a single image. All the insect MR image intensities were scaled linearly by a factor of 1.5 for better visualization unless stated otherwise.

2.3.2. MRI undersampling simulation

k-space–based simulation was employed to generate undersampled MRI data for the model training. Fully sampled brain MRI [23] k-space slices of size 256 × 256 pixels were used as ground truth. Undersampling was applied along the phase-encoding direction using a variable-density mask: the central 15 k-space lines were fully sampled, while the peripheral lines were sampled randomly with variable density, resulting in an overall sampling rate of approximately 13%–33%.

For the insect dataset, 200 fully sampled MR images of size 256 × 256 pixels served as ground truth. Each image was undersampled multiple times using independent undersampling masks, generating a total of 500 undersampled–fully sampled image pairs. In each k-space, the central 24 phase-encode lines were fully sampled, while the peripheral lines were undersampled with random variable-density pattern, resulting in an overall sampling fraction of 20%–50%. The difference in central k-space sampling between the brain and insect datasets reflects the SNR and feature content: brain MRI has higher SNR and more structural detail, allowing fewer fully sampled lines, whereas the μMRI insect data requires more central lines to preserve

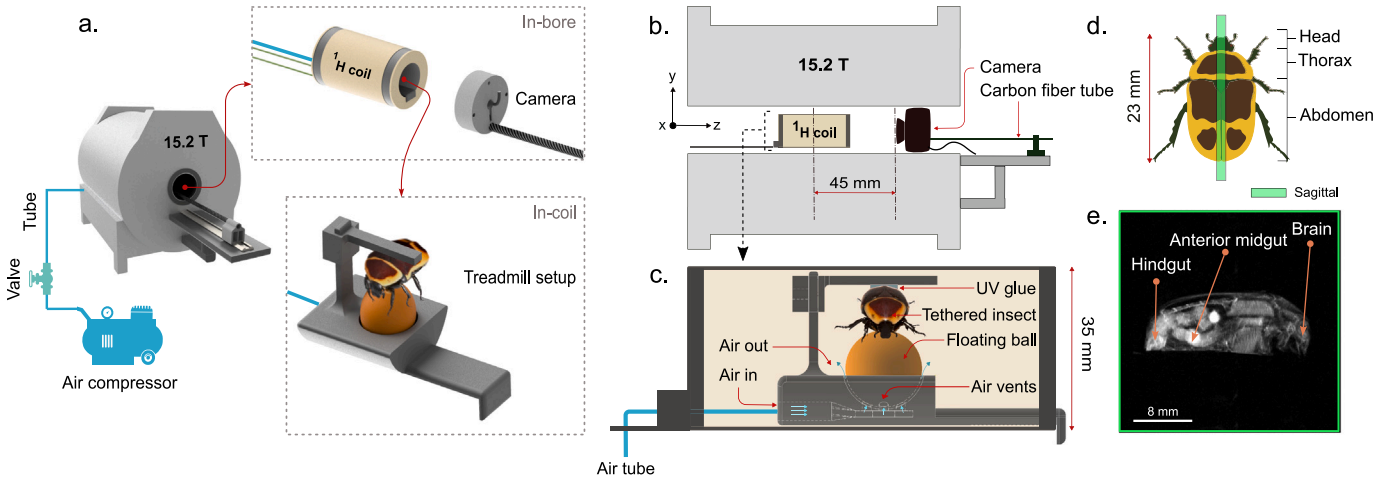

Fig. 1. *In situ* treadmill setup for MRI of a behaving insect. **(a)** Overview of the treadmill setup inside the 15.2 T magnet. **(b)** ^1H RF volume coil and MR-compatible camera inside the bore. **(c)** Schematic of a tethered active insect on the treadmill inside the coil. **(d)** Sagittal MRI slice reference position. **(e)** Sagittal MRI of an inactive insect highlighting the brain and alimentary canal.
Source: Adapted from Chenakkara et al. [5].

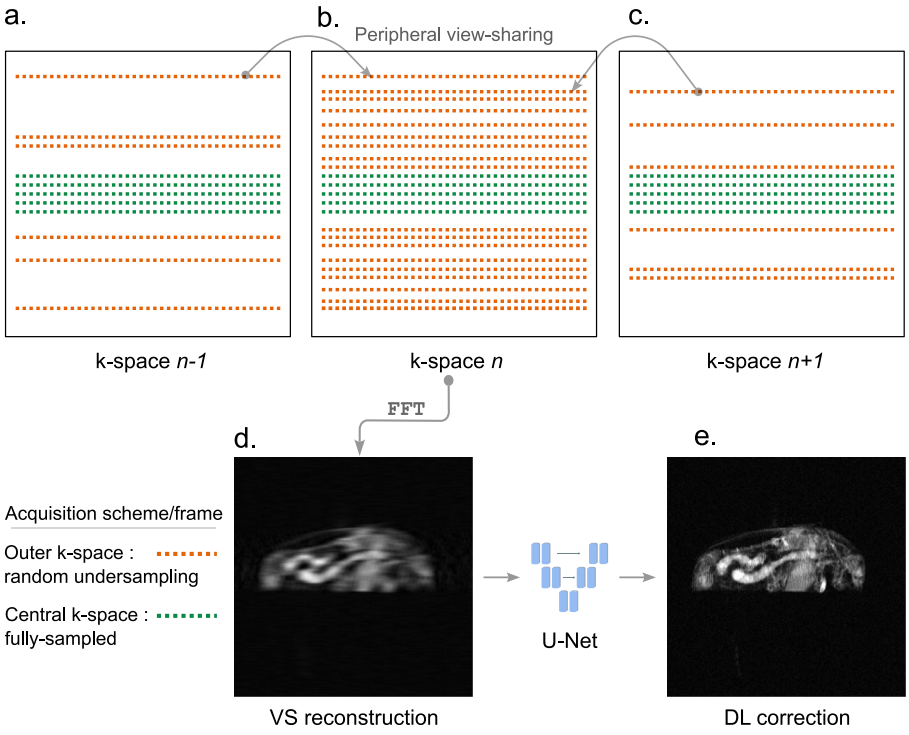

Fig. 2. Schematic representation of retrospective view-sharing (VS) with deep learning (DL)-corrected reconstruction. **(a)** Previous k-space. **(b)** Current k-space. **(c)** Next k-space. **(d)** View-shared MRI. **(e)** Deep learning-corrected MRI.

essential information. The full pipeline is illustrated in Fig. 3: (a) fully sampled magnitude image, (b) corresponding k-space magnitude, (c) undersampling mask, (d) undersampled k-space magnitude, and (e) zero-filled reconstruction magnitude image.

For the model evaluation, the dataset consisted of a simulated insect test set of 150 image pairs, which were retrospectively undersampled at effective acceleration factors of $R = 2\times$, $3\times$, and $5\times$. In all cases, additive complex Gaussian noise was added to the fully sampled k-space data before undersampling to improve robustness.

2.3.3. Deep learning model architecture and training

We used a transfer learning strategy, following our previous work [6] (Fig. 3(f) and (g)), where the model was first pretrained on a large brain MRI dataset and subsequently fine-tuned end-to-end on a smaller insect MRI dataset. The fine-tuning set was a balanced mix containing equal contributions from the brain and insect datasets. Let $x \in \mathcal{X}$ denote an undersampled MRI image with reconstruction artifacts and $y \in \mathcal{Y}$ the corresponding fully sampled reference image; the objective is to learn a mapping $f_\theta : \mathcal{X} \to \mathcal{Y}$ such that the output $\hat{y} = f_\theta(x)$ closely approximates y. The deep learning model [6] is first pretrained on the brain MRI dataset $\mathcal{D}_{\text{brain}}$ by minimizing the mean squared error (MSE) loss $\mathcal{L}_{\text{pretrain}}(\theta) = \mathbb{E}_{(x,y)}[\|f_\theta(x) - y\|_2^2]$, enabling the network to learn general features that reduce undersampling artifacts, primarily blurring. The model is then fine-tuned on the mixed dataset $\mathcal{D}_{\text{fine}}$ using a combined loss that weights SSIM [24] and MSE at 0.8:0.2, given by $\mathcal{L}_{\text{fine}}(\theta) = 0.8(1-\text{SSIM}(y,\hat{y}))+0.2\|f_\theta(x)-y\|_2^2$, which balances perceptual

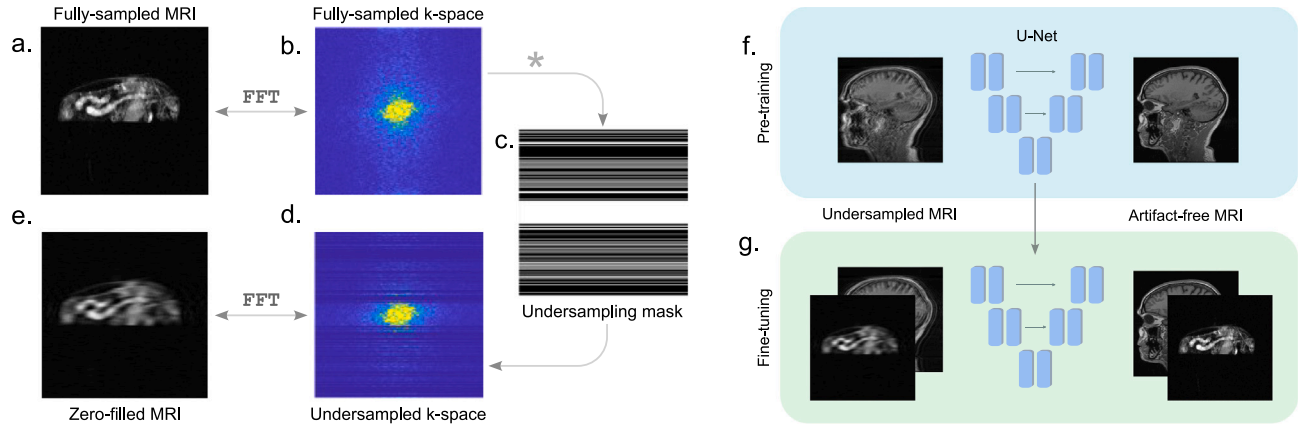

Fig. 3. Schematic representation of deep learning for undersampled MRI reconstruction artifact correction. **(a)** Fully-sampled MRI. **(b)** Fully-sampled k-space. **(c)** Undersampling mask. **(d)** Undersampled k-space. **(e)** Zero-filled (ZF) MRI reconstruction. Deep learning training pipeline **(f)** Pre-training with brain MRI dataset. **(g)** Fine-tuning with insect MRI dataset.

quality and pixel-wise accuracy. Model parameters are optimized using the Adam optimizer [25], enabling the network to adapt to insect MRI characteristics while retaining the representations learned during pretraining.

The model [6] is a modified U-Net [14] with an encoder–decoder structure and skip connections. The encoder has five hierarchical levels with feature channels [16, 32, 64, 128, 256], using 256 × 256 single-channel input. Each level employs a DoubleConv block (two 3 × 3 convolutions with batch normalization and ReLU) and 2 × 2 max-pooling for downsampling. The bottleneck has two 3 × 3 convolutions with 512 channels. The decoder upsamples via 2 × 2 transposed convolutions, followed by DoubleConv layers, with skip connections from the encoder to preserve spatial details. The output is generated through a 1 × 1 convolution, producing a single-channel 256 × 256 artifact-free MR magnitude image. The model is inherently capable of handling input sizes different from those it was trained on. Further details regarding the model architecture can be found in the Supplementary Information of [6].

For pre-training, the model was trained on a brain MRI dataset of undersampled and fully sampled image pairs with a 3000/750 training–validation split. Images were intensity-normalized and augmented via rotation and flipping to improve robustness. Training was performed as a pixel-wise regression task using MSE loss, a batch size of 12, and the Adam optimizer [25] with an initial learning rate of 1×10^{-4}. The model used early stopping with a 20-epoch patience ($\Delta = 1 \times 10^{-4}$), and the learning rate was reduced to a final value of 1×10^{-8} when the validation loss stopped improving around epoch 303. The model architecture and all the reported hyperparameters were determined empirically through experimentation.

For end-to-end fine-tuning, we trained the model on a mixed dataset consisting of 500 brain MR image pairs (a subset of the pre-training data) and 500 insect MR image pairs, using an 800/200 training–validation split. All training hyperparameters were kept identical to those used during pre-training, except for a reduced learning rate of 1×10^{-7} and a limit of 15 epochs to avoid overfitting. A combined MSE–SSIM loss function (0.2:0.8) was employed to balance pixel-level accuracy with perceptual image quality. Model performance was evaluated on both simulated and real undersampled images, which is provided in Section 3. All experiments were run on a workstation equipped with an NVIDIA RTX A5000 GPU (24 GB memory) with CUDA support, 256 GB RAM, using the Spyder 5.4.3 IDE, Python 3.9.17, and the PyTorch [26] library on Windows 10 (Microsoft, 2019).

2.4. Quantitative image assessment

We evaluated undersampling artifact correction quality of the images using two quantitative metrics. The *Structural Similarity Index Measure (SSIM)* [24] compares luminance, contrast, and structural information between a reference image x and a corrected image y:

$$\mathrm{SSIM}(x,y) = \frac{(2\mu_x\mu_y + C_1)(2\sigma_{xy} + C_2)}{(\mu_x^2 + \mu_y^2 + C_1)(\sigma_x^2 + \sigma_y^2 + C_2)}, \tag{1}$$

where μ and σ^2 denote mean intensity and variance, σ_{xy} is the covariance, and C_1, C_2 are constants. SSIM ranges from −1 to 1, with 1 indicating perfect similarity.

As a reference-free measure, *Gradient Entropy (GE)* captures randomness in normalized gradient magnitudes g_i with probability $p(g_i)$:

$$\mathrm{GE} = -\sum_i p(g_i)\log p(g_i), \tag{2}$$

where lower GE values correspond to sharper, more structured MR images [27,28]. All metrics were computed using custom Python scripts with OpenCV [29] v4.10.0, scikit-image [30] v0.21.0, and SciPy [31] v1.11.1.

2.5. Animal handling

Live adult sun beetles (*Pachnoda marginata*) were sourced from an online pet store (https://thepetfactory.de) and housed in a custom terrarium at room temperature with water and fruits as diet. The protocol for animal handling and tethering followed previously described methods [5,6]. A single beetle was used for the undersampled acquisition, initially immobilized by cooling for 15 min, and subsequently placed in a ventilated container. For tethering, a drop of UV-cured adhesive (Delo Industrial Adhesives GmbH & Co. KG, Windach, Germany) was applied to the 3D-printed PLA tether, which is then positioned on the beetle's dorsal scutellum. The adhesive was cured under a UV lamp for 10 s, after which the tethered insect was placed on the treadmill inside the RF volume coil for the MRI acquisition. After experiments, the tether was removed with a cotton swab soaked in warm water, and the beetle was euthanized after the study.

3. Results

3.1. Deep learning for undersampled MRI

3.1.1. Model evaluation on simulated data

We evaluated the fine-tuned model on a set of 150 simulated undersampled insect MR images across different acceleration factors (2×, 3×, and 5×), using structural similarity index (SSIM) and gradient entropy (GE) as quantitative metrics. The ground truth k-space was retrospectively undersampled following the strategy described in Section 2.3.2. Zero-filled (ZF) reconstructions for the acceleration factors are shown in

Table 1
Gradient entropy (GE) and structural similarity index (SSIM) for zero-filled (ZF) and deep learning (DL)–corrected reconstructions of the simulated dataset at different acceleration factors (mean ± SD, $n = 150$).

Acceleration	GE		SSIM	
	ZF	DL	ZF	DL
2×	3.230 ± 0.051	2.154 ± 0.086	0.6461 ± 0.0709	0.7585 ± 0.0707
3×	3.453 ± 0.070	2.191 ± 0.095	0.5846 ± 0.0808	0.7447 ± 0.0699
5×	3.594 ± 0.087	2.284 ± 0.110	0.5361 ± 0.0853	0.7184 ± 0.0802

Fig. 4(a–c), and their corresponding deep learning (DL) corrections are shown in Fig. 4(e–g). The fully sampled ground truth image is shown in Fig. 4(d). The quantitative image quality metrics are summarized in Table 1 and visualized as bar graphs in Fig. 4(h) and (i). The variable density undersampling predominantly introduces blurring, which is mitigated by DL correction across all tested acceleration factors. However, higher acceleration factors result in progressively smoother reconstructions, likely due to over-regularization by the network, as expected for single-coil acquisitions. Based on these observations, an acceleration factor of 2.5× was selected for the experimental acquisition in the subsequent sections.

3.2. Dynamic MRI: view-sharing with deep learning correction

The pipeline begins with undersampled k-space acquisition of a 2D slice (position reference Fig. 1(d)) across 140 repetitions, generating dynamic frames with an effective acquisition time of 1.2 s per frame, as described in Section 2.2. The k-space magnitude for a sample frame is shown in Fig. 5(a). The zero-filled (ZF) reconstruction of this frame is shown in Fig. 5(b), and the deep learning (DL)-corrected ZF reconstruction is shown in Fig. 5(c). For comparison, the view-shared (VS) k-space magnitude of the same frame is shown in Fig. 5(f), followed by its ZF reconstruction in Fig. 5(g) and the corresponding DL-corrected VS reconstruction in Fig. 5(h). The image-time profiles corresponding to the 140 frames for each of the above cases (i.e., Fig. 5(b), (c), (g), and (h)) are shown in Fig. 5(d), (e), (i), and (j), respectively. Dynamic 2D RARE images were acquired with a repetition time of 150 ms. The short TR prevents full recovery of longitudinal magnetization between excitations, resulting in frame-to-frame intensity fluctuations, as observed in Fig. 5(d) and (e). The temporal smoothening of the view-sharing step reduces the intensity oscillations (see Fig. 5(i)), while the subsequent DL-correction sharpens the final images, as evident in Fig. 5(j).

As ground-truth dynamic images are not available, we evaluate reconstruction quality using the gradient entropy (GE) metric, which is a reference-free measure. Lower GE values indicate better MR image quality. The GE values for the sample frames are provided directly in the figures. As expected, the VS reconstruction exhibits lower GE than the ZF reconstruction, and the DL correction further reduces GE for both cases. Although the added peripheral k-space lines improve spatial resolution, their lower signal-to-noise ratio (SNR) introduces additional noise into the reconstruction. The DL model effectively suppresses this noise while preserving the resolution gain. Fig. 5(k) shows the GE distribution, computed using kernel density estimation (KDE), for ZF reconstructions and their DL-corrected counterparts, where DL correction reduces GE from 3.384 ± 0.214 to 2.421 ± 0.199. Similarly, Fig. 5(l) shows the GE distribution for VS reconstructions before and after DL correction, with GE improving from 3.221 ± 0.092 to 2.228 ± 0.055. Notably, VS reconstructions exhibit lower GE than ZF even prior to DL correction, and the combination of VS and DL correction yields the lowest GE overall, demonstrating improved image quality.

3.2.1. Correlated dynamic μMRI and optical imaging

The integrated MR-compatible camera provides real-time optical images of external morphology, temporally synchronized with DL-corrected dynamic μMRI frames depicting internal anatomy (see Fig. 6). Dynamic MRI acquisition parameters are provided in Section 2.2. Image–time profiles along a selected line are shown for both modalities in Fig. 6(a) and (b). Representative frames illustrating different stride phases of the insect's abdominal pitching during tethered locomotion, with corresponding frame indices ($n = 140$) and times relative to the first displayed frame, are shown in Fig. 6(c) and (d). The final correlated video is provided as supplementary material. In tethered insect locomotion, behavioral variability reflects natural differences in movement patterns, even under controlled experimental conditions. As a result, gross abdominal motion occurs intermittently, while internal organ movement dominates the dynamic sequence. Observed instances of gross abdominal motion are indicated in Fig. 6(a) and (b).

4. Discussion and conclusion

We have demonstrated that μMRI can resolve distinct abdominal pitching dynamics in a live, tethered insect. The internal morphological dynamics revealed by MRI can be directly correlated with external morphological movements captured through the integrated optical imaging system. This multimodal approach opens the possibility for non-invasive, simultaneous visualization of internal and external abdominal kinematics during locomotion, providing insights inaccessible to conventional optical methods alone.

Dynamic and real-time MRI is typically performed using gradient-echo (GRE) or echo-planar imaging (EPI)–based sequences, often combined with advanced non-Cartesian trajectories. In the present study, however, we employed a RARE (Fast Spin-Echo) sequence to overcome the low SNR and severe susceptibility artifacts introduced by the beetle's dense chitinous exoskeleton and internal air pockets, which are limitations commonly encountered in many invertebrate models at high-field μMRI [32,33]. The spin-echo refocusing train in RARE provides intrinsically high SNR and robust suppression of signal loss and geometric distortion arising from steep susceptibility gradients at exoskeleton–tissue interfaces, whereas GRE-based non-Cartesian methods such as spiral and radial imaging are generally more prone to T_2^*-related dephasing and off-resonance blurring or distortion under these conditions. Exploring optimized non-Cartesian approaches and compensation techniques to improve robustness in this setting will be an important direction for future work.

View-sharing was incorporated as a preprocessing step to enhance the apparent information content of the undersampled k-space, thereby improving the subsequent deep learning correction and the effective temporal fidelity of the reconstructed dynamic images. In the present study, the motion model evolves slowly enough that minor view-sharing artifacts can be neglected, and the deep learning model focuses solely on mitigating undersampling artifacts. While aggressive view-sharing may lead to temporal blurring, explicitly modeling it within the deep learning framework can further improve artifact correction and the fidelity of the reconstructed images. In principle, end-to-end deep learning-based MRI reconstruction models are capable of implicitly learning temporal correlations present in dynamic data to enhance temporal resolution. However, this requires large, representative datasets, which are difficult to obtain for non-rigid, irregular or unpredictable motion, such as our case of tethered insect locomotion. View-sharing offers a classical, motion-agnostic strategy to fill missing k-space lines using information from neighboring frames, supplying the network with an improved initial estimate, and reducing the temporal footprint.

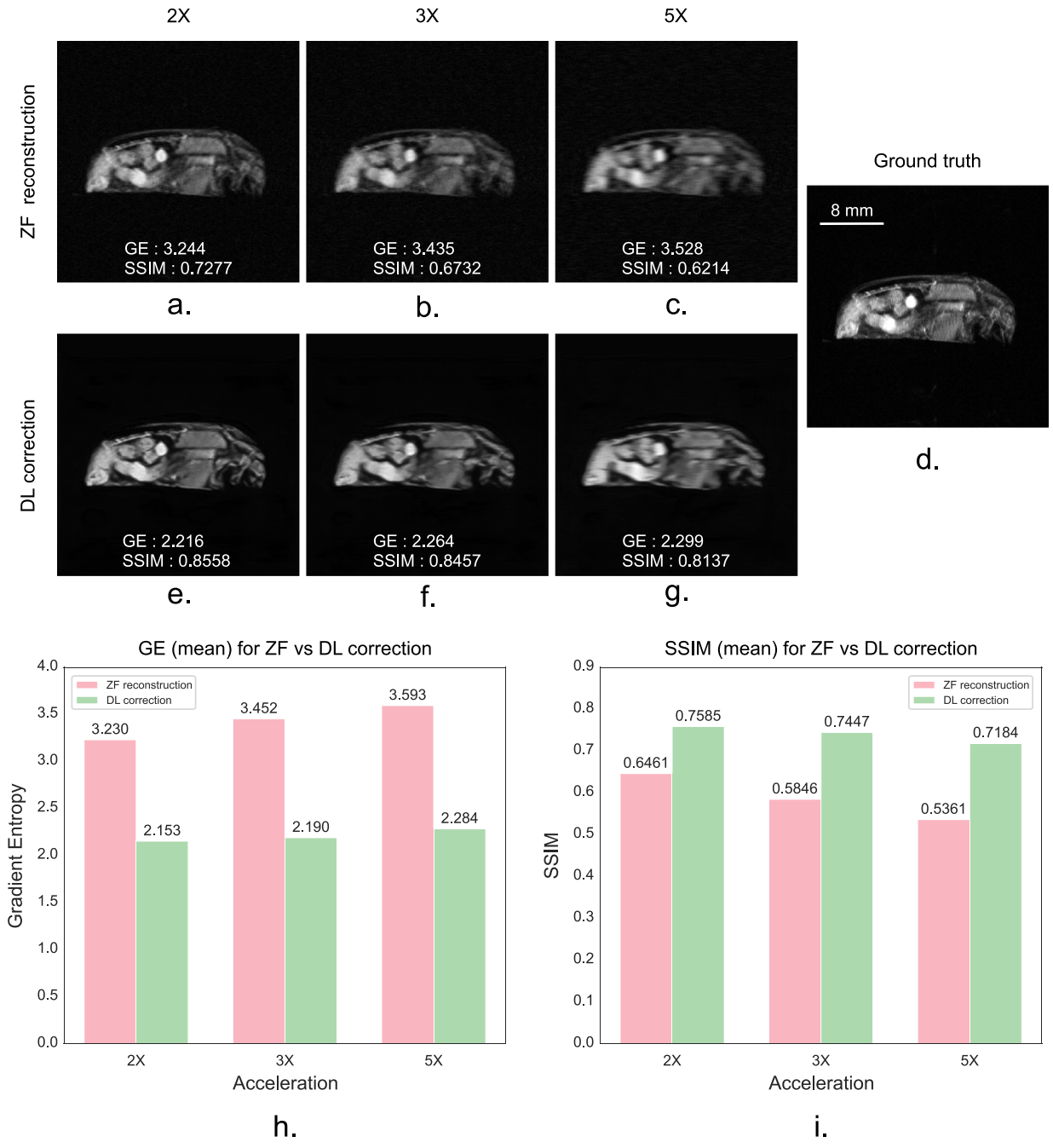

Fig. 4. Deep learning-based correction of undersampling artifacts for the simulated dataset (n = 150). **(a–c)** Zero-filled (ZF) reconstructions at 2×, 3×, and 5× acceleration, respectively. **(d)** Fully sampled ground truth image. **(e–g)** Corresponding deep learning (DL)–corrected reconstructions for 2×, 3×, and 5× acceleration. **(h)** Mean gradient entropy (GE) across acceleration factors. **(i)** Mean structural similarity index (SSIM) across acceleration factors.

Importantly, this method is not restricted to RARE sequences and can be applied to other imaging protocols with minimal adjustment.

The proposed methodology is not intended to achieve state-of-the-art high-speed dynamic MRI performance, and the resulting temporal resolution of 1.2 s per frame at 2.5× acceleration is therefore not directly comparable to advanced clinical research protocols, which benefit from larger voxels and parallel coil arrays. The significantly smaller voxel volume of the insect μMRI limits the SNR even at the ultra-high field of 15.2 T, and consequently the attainable acceleration rate. As a result, the proof-of-concept demonstrated here is suited to imaging the relatively slow abdominal dynamics of the *Pachnoda marginata*, which may not hold for a smaller, faster model organism such as *Drosophila melanogaster*. To address such cases, future work could explore strategies for achieving better temporal resolution, drawing on methods established in preclinical and clinical dynamic MRI to accommodate rapid and complex motion [8,9]. In particular, incorporating custom parallel coil arrays for μMRI could potentially allow higher acceleration factors, similar to those achievable in clinical systems.

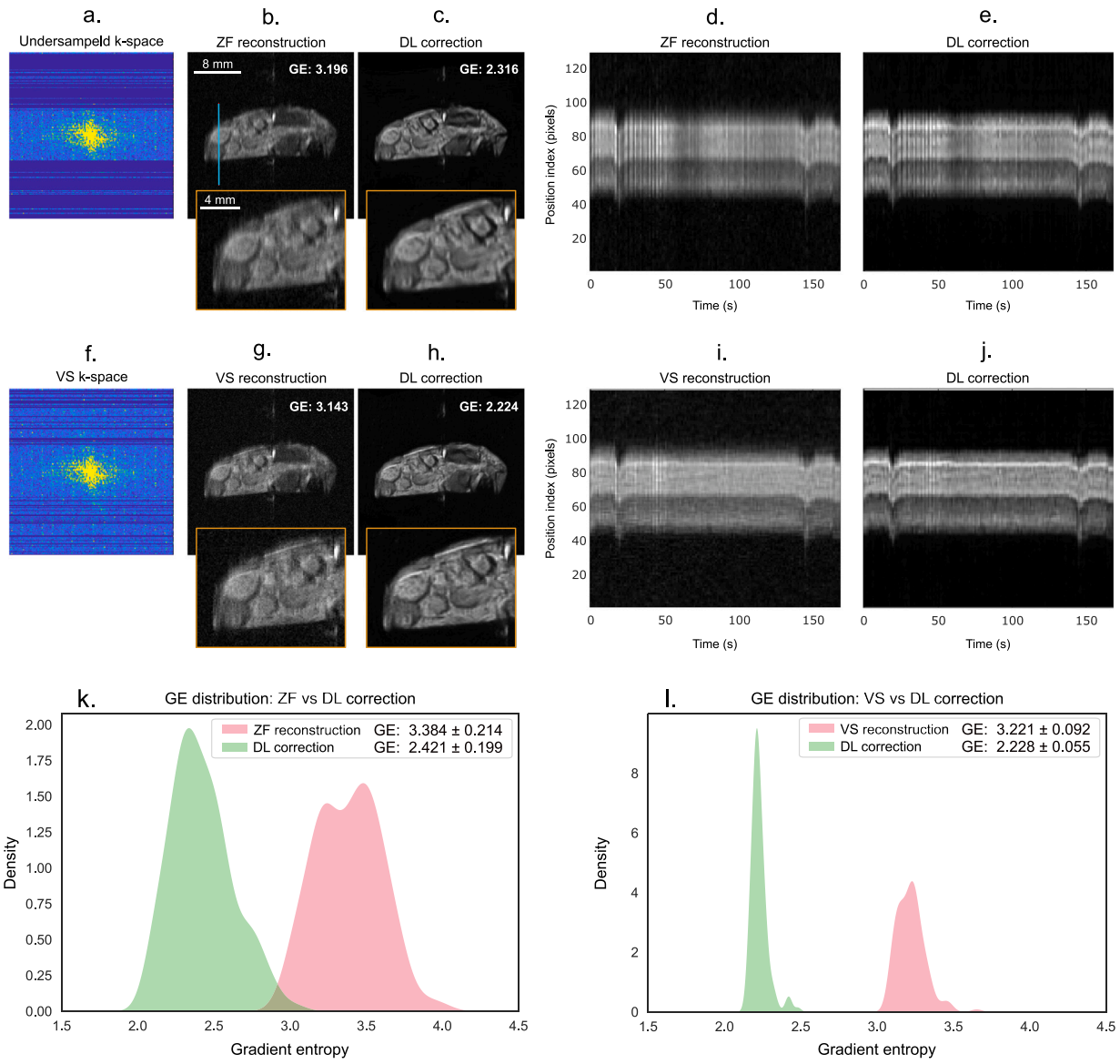

Fig. 5. Deep learning (DL)-based correction of undersampling artifacts following view-shared (VS) reconstruction ($n = 140$ dynamic MR images). **(a)** Undersampled k-space. **(b)** Zero-filled (ZF) reconstruction. **(c)** DL-corrected ZF reconstruction. **(d)** Image-time profile along the blue line in (b) for ZF reconstruction. **(e)** Corresponding image-time profile for the DL-corrected reconstruction. **(f)** VS k-space. **(g)** VS reconstruction. **(h)** DL-corrected VS reconstruction. **(i)** Image–time profile for the VS reconstruction. **(j)** Corresponding image-time profile for the DL-corrected VS reconstruction. **(k)** Gradient-entropy (GE) distribution comparing ZF and DL-corrected reconstructions. **(l)** GE distribution comparing VS and DL-corrected reconstructions.

Overall, our findings demonstrate the feasibility of dynamic *in vivo* μMRI for visualizing internal morphology across dynamic poses in tethered insects, establishing a technical foundation for future non-invasive studies of biomechanics and motor control in small invertebrate models. These results highlight the unique potential of μMRI as a powerful tool for advancing our understanding of insect locomotion and provide insights that could inform broader research in biomechanics, neuroethology, and bio-inspired robotics.

CRediT authorship contribution statement

Ajmal Chenakkara: Writing – original draft, Visualization, Investigation, Formal analysis, Data curation. **Mazin Jouda:** Writing – review & editing, Supervision, Investigation, Conceptualization. **Ulrike Wallrabe:** Writing – review & editing, Supervision, Conceptualization. **Jan G. Korvink:** Writing – review & editing, Supervision, Project administration, Funding acquisition, Conceptualization.

Declaration of competing interest

The authors declare the following financial interests/personal relationships which may be considered as potential competing interests: Jan Korvink reports a relationship with Voxalytic GmbH that includes: board membership. If there are other authors, they declare that they have no known competing financial interests or personal relationships that could have appeared to influence the work reported in this paper.

Acknowledgments

J.G.K. and M.J. acknowledge support from the ERC-SygG HiSCORE 951459, from the DFG-funded CRC 1527 HyPERiON, and partial financial support of the Helmholtz Association through the program Materials Systems Engineering – MSE.

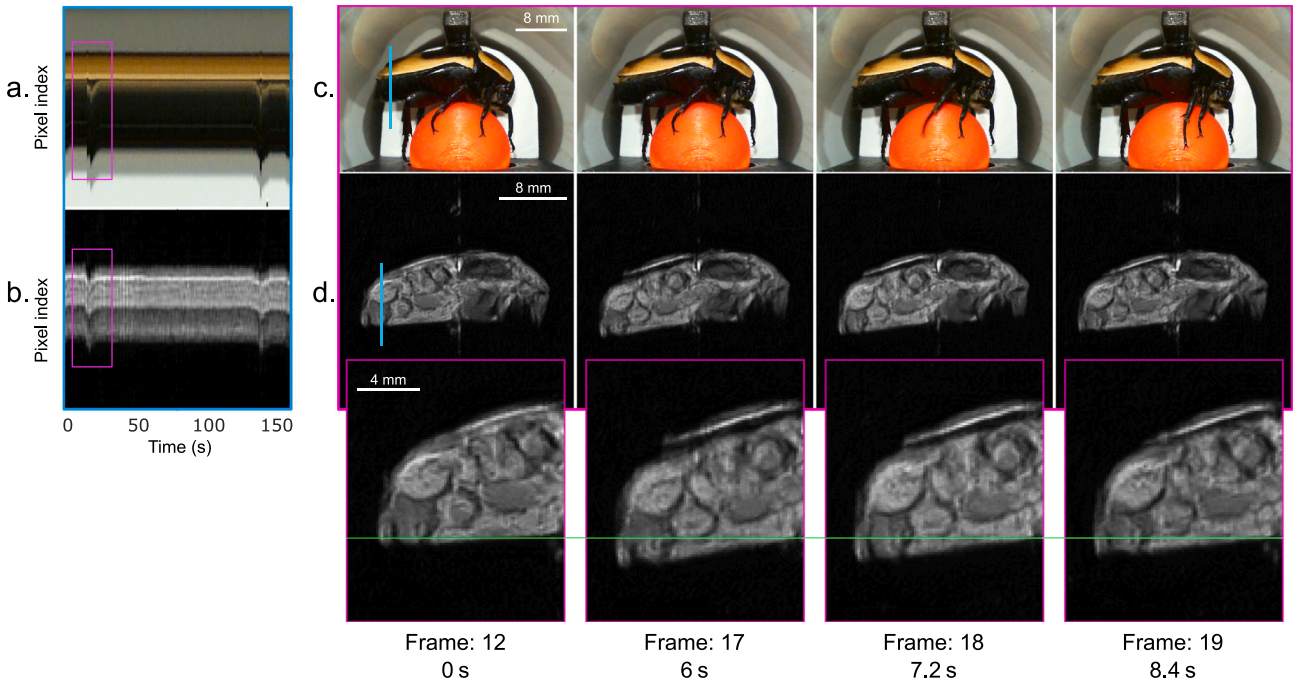

Fig. 6. Dynamic *in vivo* correlated μMRI and optical imaging of the *in situ* behaving insect. **(a)** Image–time profile extracted from the dynamic optical image sequence (n = 140). **(b)** Image–time profile extracted from the dynamic μMRI sequence (n = 140). Representative dynamic frames illustrating different stride phases of the insect's abdominal pitching during tethered locomotion, with corresponding frame indices and times (relative to the first displayed frame): **(c)** Optical image frames. **(d)** μMRI frames (green line: reference position).

Appendix A. Supplementary data

Supplementary material related to this article can be found online at https://doi.org/10.1016/j.jmr.2026.108089.

Data availability

The code and data used in this study are publicly available at: https://github.com/chenakkara/Treadmill_dynamic_MRI.git.

References

[1] J.D. Seelig, M.E. Chiappe, G.K. Lott, A. Dutta, J.E. Osborne, M.B. Reiser, V. Jayaraman, Two-photon calcium imaging from head-fixed drosophila during optomotor walking behavior, Nature Methods 7 (7) (2010) 535–540.
[2] A.F. Meyer, J. Poort, J. O'Keefe, M. Sahani, J.F. Linden, A head-mounted camera system integrates detailed behavioral monitoring with multichannel electrophysiology in freely moving mice, Neuron 100 (1) (2018) 46–60.
[3] T. dos Santos Rolo, A. Ershov, T. van de Kamp, T. Baumbach, In vivo X-ray cine-tomography for tracking morphological dynamics, Proc. Natl. Acad. Sci. 111 (11) (2014) 3921–3926.
[4] T. van de Kamp, A. Ershov, T. dos Santos Rolo, A. Riedel, T. Baumbach, Insect imaging at the ANKA synchrotron radiation facility, Èntomol. Heute 25 (2013) 147–160.
[5] A. Chenakkara, M. Jouda, U. Wallrabe, J.G. Korvink, Motion compensated magnetic resonance imaging of an active sun beetle using an in situ treadmill, Sci. Rep. 15 (1) (2025) 40340.
[6] A. Chenakkara, M. Jouda, U. Wallrabe, J.G. Korvink, Residual motion artifact removal enables dynamic μMRI of a behaving Pachnoda marginata, J. Magn. Reson. (2025) 107954.
[7] S.G. Lingala, B.P. Sutton, M.E. Miquel, K.S. Nayak, Recommendations for real-time speech MRI, J. Magn. Reson. Imaging 43 (1) (2016) 28–44.
[8] M. Burdumy, L. Traser, F. Burk, B. Richter, M. Echternach, J.G. Korvink, J. Hennig, M. Zaitsev, One-second MRI of a three-dimensional vocal tract to measure dynamic articulator modifications, J. Magn. Reson. Imaging 46 (1) (2017) 94–101.
[9] K.S. Nayak, Y. Lim, A.E. Campbell-Washburn, J. Steeden, Real-time magnetic resonance imaging, J. Magn. Reson. Imaging 55 (1) (2022) 81–99.
[10] C.J. Hardy, R.D. Darrow, M. Saranathan, R.O. Giaquinto, Y. Zhu, C.L. Dumoulin, P.A. Bottomley, Large field-of-view real-time MRI with a 32-channel system, Magn. Reson. Med.: Off. J. Int. Soc. Magn. Reson. Med. 52 (4) (2004) 878–884.
[11] J. Hamilton, D. Franson, N. Seiberlich, Recent advances in parallel imaging for MRI, Prog. Nucl. Magn. Reson. Spectrosc. 101 (2017) 71–95.
[12] S. Wang, Z. Su, L. Ying, X. Peng, S. Zhu, F. Liang, D. Feng, D. Liang, Accelerating magnetic resonance imaging via deep learning, in: 2016 IEEE 13th International Symposium on Biomedical Imaging, ISBI, IEEE, 2016, pp. 514–517.
[13] R. Heckel, M. Jacob, A. Chaudhari, O. Perlman, E. Shimron, Deep learning for accelerated and robust MRI reconstruction, Magn. Reson. Mater. Phys. Biol. Med. 37 (3) (2024) 335–368.
[14] O. Ronneberger, P. Fischer, T. Brox, U-net: Convolutional networks for biomedical image segmentation, in: International Conference on Medical Image Computing and Computer-Assisted Intervention, Springer, 2015, pp. 234–241.
[15] M.A. Bernstein, K.F. King, X.J. Zhou, Handbook of MRI Pulse Sequences, Elsevier, 2004.
[16] M. Markl, J. Hennig, Phase contrast MRI with improved temporal resolution by view sharing: k-space related velocity mapping properties, Magn. Reson. Imaging 19 (5) (2001) 669–676.
[17] E. Subashi, L. Feng, Y. Liu, S. Robertson, P. Segars, B. Driehuys, C.R. Kelsey, F.-F. Yin, R. Otazo, J. Cai, View-sharing for 4D magnetic resonance imaging with randomized projection-encoding enables improvements of respiratory motion imaging for treatment planning in abdominothoracic radiotherapy, Phys. Imaging Radiat. Oncol. 25 (2023) 100409.
[18] L.A. Tudorica, K.Y. Oh, N. Roy, M.D. Kettler, Y. Chen, S.L. Hemmingson, A. Afzal, J.W. Grinstead, G. Laub, X. Li, et al., A feasible high spatiotemporal resolution breast DCE-MRI protocol for clinical settings, Magn. Reson. Imaging 30 (9) (2012) 1257–1267.
[19] F.R. Korosec, R. Frayne, T.M. Grist, C.A. Mistretta, Time-resolved contrast-enhanced 3D MR angiography, Magn. Reson. Med. 36 (3) (1996) 345–351.
[20] E. Levine, B. Daniel, S. Vasanawala, B. Hargreaves, M. Saranathan, 3D cartesian MRI with compressed sensing and variable view sharing using complementary poisson-disc sampling, Magn. Reson. Med. 77 (5) (2017) 1774–1785.
[21] S. Rapacchi, Y. Natsuaki, A. Plotnik, S. Gabriel, G. Laub, J.P. Finn, P. Hu, Reducing view-sharing using compressed sensing in time-resolved contrast-enhanced magnetic resonance angiography, Magn. Reson. Med. 74 (2) (2015) 474–481.
[22] J. Hennig, A. Nauerth, H. Friedburg, RARE imaging: A fast imaging method for clinical MR, Magn. Reson. Med. 3 (6) (1986) 823–833, http://dx.doi.org/10.1002/MRM.1910030602.
[23] R. Souza, O. Lucena, J. Garrafa, D. Gobbi, M. Saluzzi, S. Appenzeller, L. Rittner, R. Frayne, R. Lotufo, An open, multi-vendor, multi-field-strength brain MR dataset and analysis of publicly available skull stripping methods agreement, NeuroImage 170 (2018) 482–494.
[24] Z. Wang, A.C. Bovik, H.R. Sheikh, E.P. Simoncelli, Image quality assessment: from error visibility to structural similarity, IEEE Trans. Image Process. 13 (4) (2004) 600–612.

[25] D.P. Kingma, J. Ba, Adam: A method for stochastic optimization, 2014, arXiv preprint arXiv:1412.6980.
[26] A. Paszke, S. Gross, F. Massa, A. Lerer, J. Bradbury, G. Chanan, T. Killeen, Z. Lin, N. Gimelshein, L. Antiga, et al., Pytorch: An imperative style, high-performance deep learning library, Adv. Neural Inf. Process. Syst. 32 (2019).
[27] E. Marchetto, H. Eichhorn, D. Gallichan, J.A. Schnabel, M. Ganz, Agreement of image quality metrics with radiological evaluation in the presence of motion artifacts, 2024, arXiv preprint arXiv:2412.18389.
[28] K.P. McGee, A. Manduca, J.P. Felmlee, S.J. Riederer, R.L. Ehman, Image metric-based correction (autocorrection) of motion effects: analysis of image metrics, J. Magn. Reson. Imaging: Off. J. Int. Soc. Magn. Reson. Med. 11 (2) (2000) 174–181.
[29] G. Bradski, The OpenCV library, Dr. Dobb's J. Softw. Tools (2000).
[30] S. Van der Walt, J.L. Schönberger, J. Nunez-Iglesias, F. Boulogne, J.D. Warner, N. Yager, E. Gouillart, T. Yu, Scikit-image: image processing in Python, PeerJ 2 (2014) e453.
[31] P. Virtanen, R. Gommers, T.E. Oliphant, M. Haberland, T. Reddy, D. Cournapeau, E. Burovski, P. Peterson, W. Weckesser, J. Bright, et al., Scipy 1.0: fundamental algorithms for scientific computing in python, Nature Methods 17 (3) (2020) 261–272.
[32] S. Wecker, T. Hörnschemeyer, M. Hoehn, Investigation of insect morphology by MRI: Assessment of spatial and temporal resolution, Magn. Reson. Imaging 20 (1) (2002) 105–111.
[33] A. Ziegler, M. Kunth, S. Mueller, C. Bock, R. Pohmann, L. Schröder, C. Faber, G. Giribet, Application of magnetic resonance imaging in zoology, Zoomorphology 130 (2011) 227–254.